RESEARCH ARTICLE | AUGUST 01 2025

Near-field infrared imaging of polar domain walls in Ni_3TeO_6

Special Collection: Ferroic Materials, Domains, and Domain Walls: Bridging Fundamentals with Next-Generation Technology

Ashley M. Sargent ; Kevin A. Smith ; Xianghan Xu ; Kai Du ; Sang-Wook Cheong ;
Lukas Wehmeier ; G. L. Carr ; Janice L. Musfeldt ✉

Check for updates

CHORUS

View Online

Export Citation

Articles You May Be Interested In

Interlocked chiral/polar domain walls and large optical rotation in Ni_3TeO_6

APL Mater. (July 2015)

X-ray nanospectroscopy for attogram-scale two-dimensional nanomaterials using photoelectron emission microscopy

AIP Conf. Proc. (June 2010)

Rapidly frequency-tuneable, in-vacuum, and magnetic levitation chopper for fast modulation of infrared light

Rev. Sci. Instrum. (August 2022)

Near-field infrared imaging of polar domain walls in Ni₃TeO₆

Ashley M. Sargent,[1] Kevin A. Smith,[1] Xianghan Xu,[2] Kai Du,[2] Sang-Wook Cheong,[2]
Lukas Wehmeier,[3] G. L. Carr,[3] and Janice L. Musfeldt[1,4,a)]

AFFILIATIONS

[1] Department of Chemistry, University of Tennessee, Knoxville, Knoxville, Tennessee 37996, USA

[2] Keck Center for Quantum Magnetism and Department of Physics and Astronomy, Rutgers University, Piscataway,
New Jersey 08854, USA

[3] National Synchrotron Light Source II, Brookhaven National Laboratory, Upton, New York 11973, USA

[4] Department of Physics and Astronomy, University of Tennessee, Knoxville, Knoxville, Tennessee 37996 USA

Note: This paper is part of the Special Topic, Ferroic Materials, Domains, and Domain Walls: Bridging Fundamentals with
Next-Generation Technology.

a)Author to whom correspondence should be addressed: musfeldt@utk.edu

ABSTRACT

Domain walls are leading platforms for the development of ultra-low power switching and memory devices due to their potential to be moved, created, and erased in real time and to mitigate heat flux. Interface vs wavelength size effects unfortunately preclude the measurement of phonons by traditional spectroscopic techniques, so it has been challenging to unravel the primary excitations of the lattice and the symmetries that they represent across these functional interfaces. In this work, we employ synchrotron-based near-field infrared nanospectroscopy to image polar domain walls in multiferroic Ni₃TeO₆. This is a unique platform because, in addition to hosting polar and chiral domains that are interlocked with one another, Ni₃TeO₆ displays both charged and neutral interfaces depending upon the direction allowing the development of structure–property relations. From a local structure and a strain point of view, we find charged walls that are twice as wide as neutral walls as well as strong frequency shifts of vibrational modes across the charged walls. The near-field amplitude drops across the walls as well. We discuss these trends in terms of polarization and chirality as well as phonon lifetimes at functional interfaces.

I. INTRODUCTION

Electric polarization is a desirable material property because it can be readily manipulated and controlled. Often, this parameter is associated with the rich domain structure in ferroelectrics where the spontaneous polarization direction switches across the interfacial domain walls.[1–3] Ferroelectric walls can be created in varying densities and moved and erased in real time with the application of external stimuli.[4,5] Naturally, they are attracting considerable attention as platforms for logic, sensing, and neuromorphic computing.[2,4,6–8] In these systems, both charged and neutral domain walls can be formed depending upon the orientation of the polarization in adjacent domains. A residual bound charge at the wall, typically from head-to-head or tail-to-tail orientations of the polarization, will create a charged wall, whereas an antiparallel orientation with no bound charge will result in a neutral wall.[9] Of course, polar systems fall into two broad categories: ferroelectrics and pyroelectrics. The latter has a polarization and even domain walls, but it is not switchable and, in fact, replies on temperature change to modulate the polarization. Still, they manifest useful characteristics similar to their ferroelectric counterparts providing an additional platform for examining the properties of polar domain walls.

Domain wall structures have been explored using different imaging techniques, including force and electron microscopies.[10–12] It turns out that polar interfaces host a variety of exciting properties, including changes in symmetry and conductivity that differ from the bulk.[13–16] That said, domain walls are under-explored by

spectroscopic methods.[17–19] This is because the spatial resolution of most spectroscopic techniques tends to be restricted by the Abbe diffraction limit, which is typically a few micrometers. In order to probe the dynamics of nanoscale interface like domain walls, we need to reach beyond traditional spectroscopic approaches toward more novel instrumentation such as synchrotron-based near-field infrared spectroscopy [Fig. 1(a)]. The latter is a tip-based technique that combines atomic force microscopy (AFM) and Fourier transform infrared spectroscopy to beat the natural diffraction limit of light to enable real space imaging at the nano-scale.[20] Use of a high-brightness accelerator-based source rather than a laser enables broad band infrared imaging even into the far infrared.[21–23] The fundamental excitations of the lattice tend to reside in this frequency region—especially in materials with heavy centers.

Synchrotron-based near-field infrared spectroscopy has been employed to examine both proper and hybrid-improper ferroelectrics.[24,25] Naturally, there is interest in extending toward more complex systems. Ni_3TeO_6 is a polar antiferromagnet ($T_N = 53$ K) crystallizing in the $R3$ space group.[26] It hosts a corundum-like structure with three inequivalent nickel sites (designated $Ni_{(i)}$, $Ni_{(ii)}$, and $Ni_{(iii)}$) and tellurium where the metal centers are organized along c [Fig. 1(b)]. $TeO_6–Ni_{(iii)}O_6$ and $Ni_{(i)}O_6–Ni_{(ii)}O_6$ octahedra are edge sharing within each layer, and $Ni_{(ii)}O_6$ and $Ni_{(iii)}O_6$ are face sharing between layers. Chirality arises along c, the polar

axis, as a consequence of the $120°$ rotation of the 3 NiO_6 and 1 TeO_6 octahedra that make up the basic building blocks of Ni_3TeO_6 [Fig. 1(c)].[27] This results in both left- and right-handed incommensurate chiral helices from which an overall net chirality arises.[28] The chiral nature of these domains is easy to visualize using transmission polarized optical microscopy. The opposing crystal regions appear as dark and light green areas; the interfaces correspond to domain walls—a consequence of the interlocked polarization and chirality. Ni_3TeO_6 is, therefore, a superb platform for unveiling interlocked polar and chiral domains,[28] colossal magnetoelectric effects,[29,30] and nonreciprocal directional dichroism.[31–33] We point out that while this system is polar, it is not switchable.

The interlocked domain walls in Ni_3TeO_6 offer an exceptional imaging opportunity. The neutral, polar, out-of-plane domain walls, originating in the ab-plane, meander through the sample and when exposed along c can end up in a charged orientation where the polarization and chirality are both in-plane. At the same time, neutral domain walls oriented linearly along c provide a chance to analyze the spectral contrast and simultaneously unravel structure–property relations in an unusual setting. Synchrotron-based near-field infrared imaging reveals an especially large frequency shift in a c-polarized vibrational mode at charged domain walls. It is significantly larger than those associated with the neutral walls. In comparing these trends, we resolve the implications of both polarization and on-end chirality on the domain wall properties. The ability to quantify the consequences of charge accumulation at a functional interface in terms of a phonon lifetime opens new avenues of exploration in heat management as well.[11,34–37]

II. METHODS

A. Crystal growth and domain wall imaging

Thick single crystals of Ni_3TeO_6 were grown by flux methods to expose the c-axis as previously described.[38] Domain walls were exposed and enhanced using vibratory polishing in a fine colloidal silica. Areas of both charged ab and neutral c polar walls were identified and imaged using piezoresponse force microscopy (PFM) and an optical microscope under cross-polarized light. These optical images and the structures revealed were used as a navigation tool in order to identify topographical regions of interest to scan using atomic force microscopy, which allowed us to locate and examine the spectroscopic response of the polar domain walls.

B. Far-field spectroscopies

The near-field response was compared to that of traditional techniques. Far-field infrared measurements were performed over the frequency range of $20–700$ cm^{-1} using a Bruker IFS 113V spectrometer in a transmittance mode on a polycrystalline paraffin pellet. Absorption was calculated as $\alpha(\omega) = -\frac{1}{dh}\ln(\mathcal{T}(\omega))$, where d is the sample thickness, h is the concentration, and $\mathcal{T}(\omega)$ is the measured transmittance. Additionally, complementary single crystal Raman scattering measurements were performed using a Horiba LabRam HR Evolution spectrometer equipped with a $50\times$ objective, 1800 g/mm grating, and a 532 nm laser at a power of approximately $35\,\mu$W. Aperture-based techniques are diffraction limited and therefore have a spot size on the order of several micrometers.

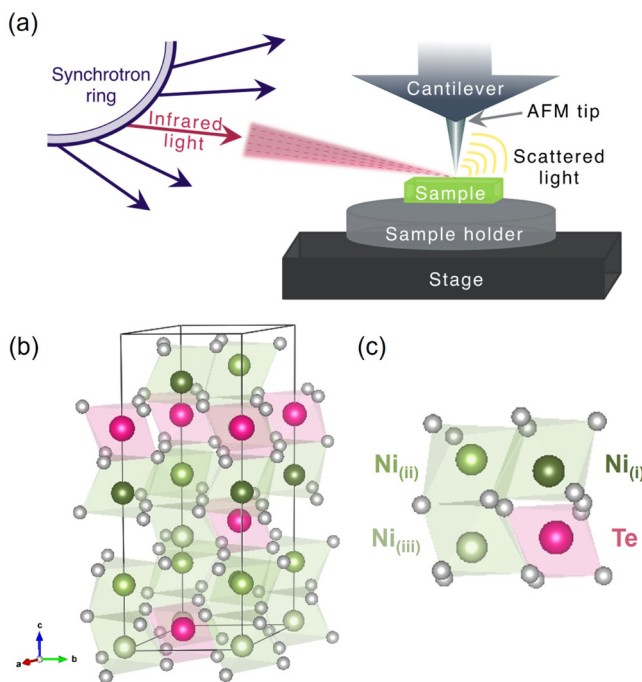**FIG. 1.** (a) Diagram of the synchrotron-based near-field infrared setup. The spacial resolution is on the order of 20×20 nm^2. (b) Crystal structure of Ni_3TeO_6. (c) The basic building block of Ni_3TeO_6 is shown with each unique metal center indicated. Chirality in this material originates from a $120°$ rotation of neighboring building block units along c.[27,28]

Consequently, the far-field spectrum provides an averaged response of the crystal over multiple domains.

C. Synchrotron-based near-field infrared spectroscopy

Near-field infrared spectroscopy was performed at beamline 22-IR-2 at the National Synchrotron Light Source II, Brookhaven National Laboratory.[20,22,23] Our measurements focused on the second harmonic signal between 250 and 800 cm^{-1} in order to capture the behavior of the infrared-active phonons in this system. This work was performed at room temperature due to the robustness of the polar domain walls in Ni_3TeO_6. The collected spectra are normalized to a gold reference mirror. The spatial resolution of this tip-based technique is approximately 20×20 nm^2. Both point and line scans were carried out in this work. Each line scan was approximately a micrometer in length, and a 20 nm step size was employed. Additional information is available in the supplementary material.

III. RESULTS AND DISCUSSION

A. Locating neutral and charged walls

Atomic force microscopy directly images surface textures in different types of materials, including insulating stripes in V_2O_3[39] and ferroelastic domain walls in the hybrid-improper ferroelectric $Ca_3Ti_2O_7$.[40] In both materials, there is a structural component associated with these textures, which is necessary for this type of imaging. In AFM, domain walls appear as very distinct linear deformations in the topographical image with relatively small amplitude changes—generally just tens of nanometers. In terms of direction and location, the ferroelectric/ferroelastic walls appear to be in good agreement with other imaging techniques, including optical microscopy and other tip-based methods, such as PFM. However, in materials where the walls are purely ferroelectric with no additional strain, as is the case in h-(Lu, Sc)FeO$_3$,[24] these walls cannot be visualized

using AFM and as such rely on the use of markers or structural defects on the sample surface to navigate and locate.

When Ni_3TeO_6 is preferentially grown to expose the c-direction, the crystal reveals both 180° polar charged walls originating from the ab-plane and non-charged c-walls. In neutral walls, the polarization directions of $+P$ and $-P$ are aligned antiparallel to one another across the wall. In the charged walls, the polarization is oriented in either head-to-head or tail-to-tail alignment. A representation of both antiparallel and head-to-head walls is shown in Fig. 2(a). Due to the interlocking,[28] the chiral helices must be aligned edge-to-edge at the neutral walls and end-to-end at the charged walls. The general locations of these walls can be determined using the transmission polarized optical images as shown in Fig. 2(b), where the polarization and the chiral axis along c are in the plane of the exposed crystal face. To perform near-field infrared measurements on each of these walls, they must be specifically located using AFM. Scans were methodically performed using intermittent tapping from the edge of the sample down through the region where the neutral walls should be located [Fig. 2(b), blue box] and back up as represented by the white arrows; however, no walls could be topographically visualized. This is because polarization is completely compensated in these walls leaving no residual bound charge and, thus, no structural deformation.[11,13] The camera used in the AFM is not equipped with polarizers, so in order to find the neutral walls, we scoured the sample surface for defects. Due to the vibratory polishing method used to expose the walls, the sample surface was incredibly smooth and virtually defect free. Therefore, previously performed PFM scans and optical images were overlaid with a view of the cantilever positioned over the sample in the AFM to narrow down the location of the walls. An example of this method is shown in Fig. 2(c). From their overlapping, 1–1.5 micrometer near-field infrared line scans were performed using a step size of 20 nm to capture the spectroscopic signature of the neutral wall. Multiple charged walls were imaged
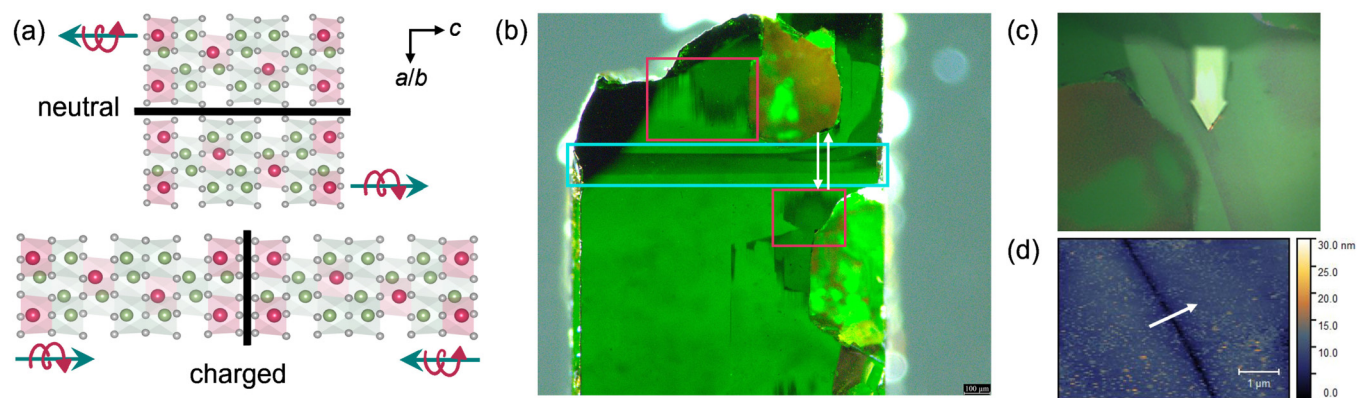
FIG. 2. (a) General structural relationship between adjacent domains for both neutral and charged walls. Pink and green arrows show the orientation of chirality and polarization, respectively. For the purposes of this discussion, the orientation of the chiral helices across a neutral wall is referred to as being edge-to-edge to one another, while the chiral helices across a charged wall are described as being on-end to one another. (b) Polarized optical transmission reveals the general location of both charged ab walls (pink boxes) and neutral c walls (blue box). The white arrows show the approximate path of AFM scans performed in an attempt to visualize the neutral walls. (c) An image of the cantilever position above the sample is overlaid on an optical image to show the location of our neutral wall line scans. (d) Representative AFM image of a charged wall. The white arrow indicates the location and direction of our near-field line scan.

using AFM in different regions of the sample. A representative AFM image is shown in Fig. 2(d). These polar walls can be topographically visualized, which indicates that more substantial structural distortion must be present to stabilize the bound charge.

B. Identifying relevant phonon modes in Ni₃TeO₆

In optical images of the crystal, regions of light and dark green are indicative of opposing chiral domains.[28] Near-field infrared point scans were taken in both regions of chirality, and they were confirmed to have the same spectroscopic signature. A representative near-field point scan was compared to far-field infrared and Raman spectra, as well as previously reported DFT-calculated phonon frequencies (Fig. S1 in the supplementary material).[41] Both the near-field amplitude and phase, corresponding to the real and imaginary parts of the near-field signal, are included for completeness.[20,42] The predicted phonons are in good agreement with the experimental spectra. As with other materials with a $R3$ structure, all of the optical modes in Ni₃TeO₆ are both infrared and Raman active. In the infrared response between 300 and 700 cm⁻¹, many of the modes overlap making it difficult to extract the precise phonon position. Phonon frequencies correlating to a charged wall, mode symmetries, and displacement patterns are listed in Table I.

C. Near-field imaging of domain walls

We performed multiple near-field infrared line scans across charged ab polar domain walls located in different regions of the crystal. Each of these scans yielded consistent results. The typical near-field response for these walls is shown in Figs. 3 and 4. Five regions of pronounced phonon intensity are highlighted by the contour plot in Fig. 3(a). Here, the near-field frequency is plotted as a function of distance traveled across a one micrometer line scan where the color scale represents the near-field amplitude. A near-field amplitude change and hardening are apparent in multiple modes as the walls are crossed. The contour plot reveals the width of the charged wall to be approximately 80 nm. All of the charged walls measured fall within the range of 80–100 nm in width.

Additionally, near-field amplitude is plotted as a function of distance in Fig. 4(a), which further highlights the amplitude change across the wall. The fixed distance plot in Fig. 4(b) provides a more ubiquitous representation of the data where a spectrum averaged over the width of the wall is compared to an averaged region from within the adjacent domain. A difference spectrum is also plotted for clarity. The amplitude decreases most strongly at 470 cm⁻¹, which is assigned to a stretching mode where Ni$_{(i)}$, Ni$_{(iii)}$, and Te are displaced down along c, while Ni$_{(ii)}$ remains stationary. Conversely, at 596 cm⁻¹, assigned to an in-plane contraction of the oxygens around the metal centers, there is nearly no observable amplitude difference suggesting that this mode is resilient to changes at the charged wall. At the interface, considerable hardening of 3 and 5.6 cm⁻¹ takes place in the modes at 470 and 543 cm⁻¹, respectively (Table I). These frequency shifts are consistent with increases in the force constants of approximately 1%. The largest is highlighted in Fig. 4(c).

Near-field infrared line scans were also performed across neutral c-oriented domain walls. Once again, each wall had a consistent response, and a representative wall is subsequently shown. The contour plot in Fig. 3(b) displays the near-field infrared frequency plotted as a function of distance traveled along the line scan. The near-field amplitude, represented by the color scale, decreases as the wall is approached near 330 nm. The decrease in amplitude here is similar to that of the charged walls and exhibits the characteristic pinching shape; however, it is only half as thick, with a width of approximately 40 nm. This is consistent for all of the neutral walls that we measured. The fixed frequency plot in Fig. 4(d) is similar in shape to what we find for the charged wall. As the wall is crossed, the amplitude decreases and flattens out to a local minimum before increasing again. The change in amplitude is less significant in the fixed distance plot for the neutral wall [Fig. 4(e)] than for the charged wall. Slight hardening was observed in some cases (Fig. S2 in the supplementary material); however, these shifts are relatively small and fall below the sensitivity limit of our instrument. Note that the magnitude of the change at the wall varies between the two spectra; however, the difference spectra maintain a similar shape.

TABLE I. Approximate experimental phonon frequencies (taken from a charged wall), mode symmetries, and displacement patterns for Ni₃TeO₆. The abbreviations u, d, l, and r encode displacement patterns of up and down (along c) and left and right (in the ab-plane), respectively, for the metal centers in order Ni$_{(i)}$–Ni$_{(ii)}$–Ni$_{(iii)}$–Te. A "–" indicates essentially no change. Compressions, contractions, and rotations are also listed.[41] The frequency shift, $\Delta\omega$, at the wall is indicated for both the charged and neutral walls.

| ω (cm⁻¹)	Mode symmetries	Mode displacement patterns	$\Delta\omega$ (cm⁻¹)	
			Charged	Neutral
362	E	oct. compression ab	0	0
366	A	udud; oct. compression c	0	0
394	A	oct. twist	0	0
453	A	d-dd + oct. twist	0	0
470	E	oct. compression ab + twist	3	0
523	E	oct. twist ab	0	0
543	A	oct. contraction + rotation c	5.6	2.3
596	E	oct. contraction $a(b)$	0	1
645	A	oct. axial stretching	0	0
672	E	oct. contraction $(a+b)(a-b)$	0	2.1
688	A	oct. asymmetric stretching	0	0
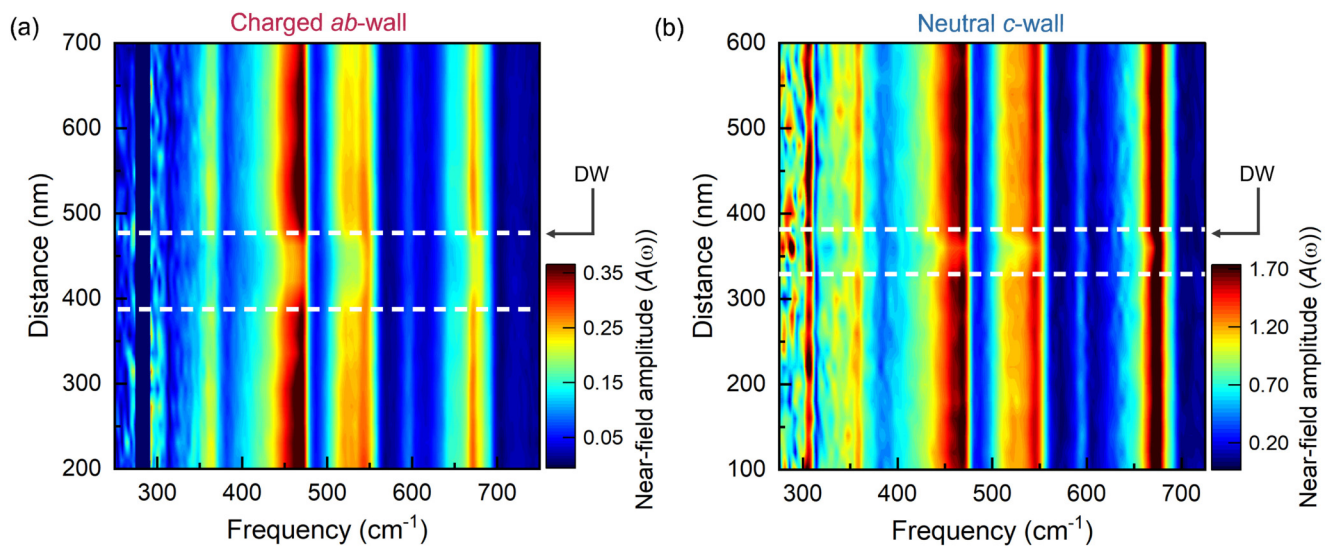
FIG. 3. Contour plots of the near-field amplitude across (a) charged and (b) neutral domain walls in Ni_3TeO_6 at room temperature. Here, the distance traveled along the path of the line scan is plotted against the frequency where the near-field amplitude is described by the color scale. The dashed white lines indicate the bounds of the walls.

The considerable differences between the two types of walls are useful for unraveling the complex relationship between polarization and chirality in Ni_3TeO_6 where the orientation of the chirality is interlocked with that of the polarization. For a neutral wall, opposite chiral helices are oriented edge-to-edge, whereas in charged walls, they are on-end to one another. The polarization orientation in Ni_3TeO_6 originates from the off-centering of $Ni_{(i)}$/$Ni_{(iii)}$ from $Ni_{(ii)}$/Te, where the displacement of the latter is greater. For the neutral domain walls, the width is significantly narrower than for the charged wall. This suggests that when the lattice is oriented so that the chiral and polar axes are edge-to-edge and antiparallel to one another, the interface is softer allowing for a faster evolution of polarization and chirality (over a shorter distance). The larger overall change in the near-field amplitude at the charged walls is due to the stiffer interface resulting from the structural stabilization required to maintain a bound charge at the wall. This suggests that neutral walls, having less of an energy cost, are likely more prevalent throughout the sample.[43,44] In both types of walls, the phonon modes between 450 and 480 cm^{-1} appear to be directly involved in strain relief at the wall as indicated by the significant amplitude changes. The greatest frequency shifts are seen at the charged walls. Although some of the frequency shifts at the neutral walls are below our sensitivity, there are many modes that do not harden suggesting that these shifts are meaningful and may be highly informative. Based on the direction of the polarization axis, phonon hardening would be expected in the modes along c if the hardening was strictly polarization driven. Yet, the neutral walls have nearly equivalent hardening in displacement patterns related to both c and ab. Another consideration is the orientation of the chiral helices at the interface. At the neutral walls, polarization causes hardening in the displacement associated with the octahedral contraction and rotation

around c as is expected due to the polarization orientation; however, there are also frequency shifts associated with modes that displace solely in ab. This indicates that the additional strain caused by the chirality at the interface also plays a role in the magnitude of the hardening at the walls. It is reasonable that the stiffer on-end helices of the charged walls would have a greater impact on the frequency shift than the edge-to-edge helices of the neutral walls. The mode at 470 cm^{-1} related to the octahedral compression and twist correlates to tightening of the chiral helices, which creates a more strained interface at the charged walls. Similarly, the on-end chirality accounts for the substantial 5.6 cm^{-1} hardening at the charged walls in the mode corresponding to contraction of the Ni (iii) and Te metal centers along and oxygen rotations around c.

D. Estimating phonon lifetimes at the domain walls

There are a number of properties, including heat capacity, thermal expansion/contraction, and heat dissipation that derive from phononic behavior.[45–47] One way to quantify specific contributions to these effects is via phonon lifetimes.[48] The expression is $\tau_{ph} = \hbar/\Gamma$, where Γ is the full width at half-maximum for each phonon. The phonon lifetime τ_{ph} is a measure of how long the phonon propagates before a scattering event occurs. A large τ_{ph} is consistent with a long mean free path, efficient heat dissipation, and high thermal conductivity. In practice, it can be challenging to evaluate τ_{ph} from the near-field response due to sensitivity issues. This is because one has to extract the linewidth Γ with high reliability in a spatially resolved manner. It turns out that if we consider the relative change in the phonon lifetime between the domain and domain wall, defined as $\Delta\tau_{ph}$, the uncertainty is dramatically reduced. Evaluating only the higher frequency phonons, which are
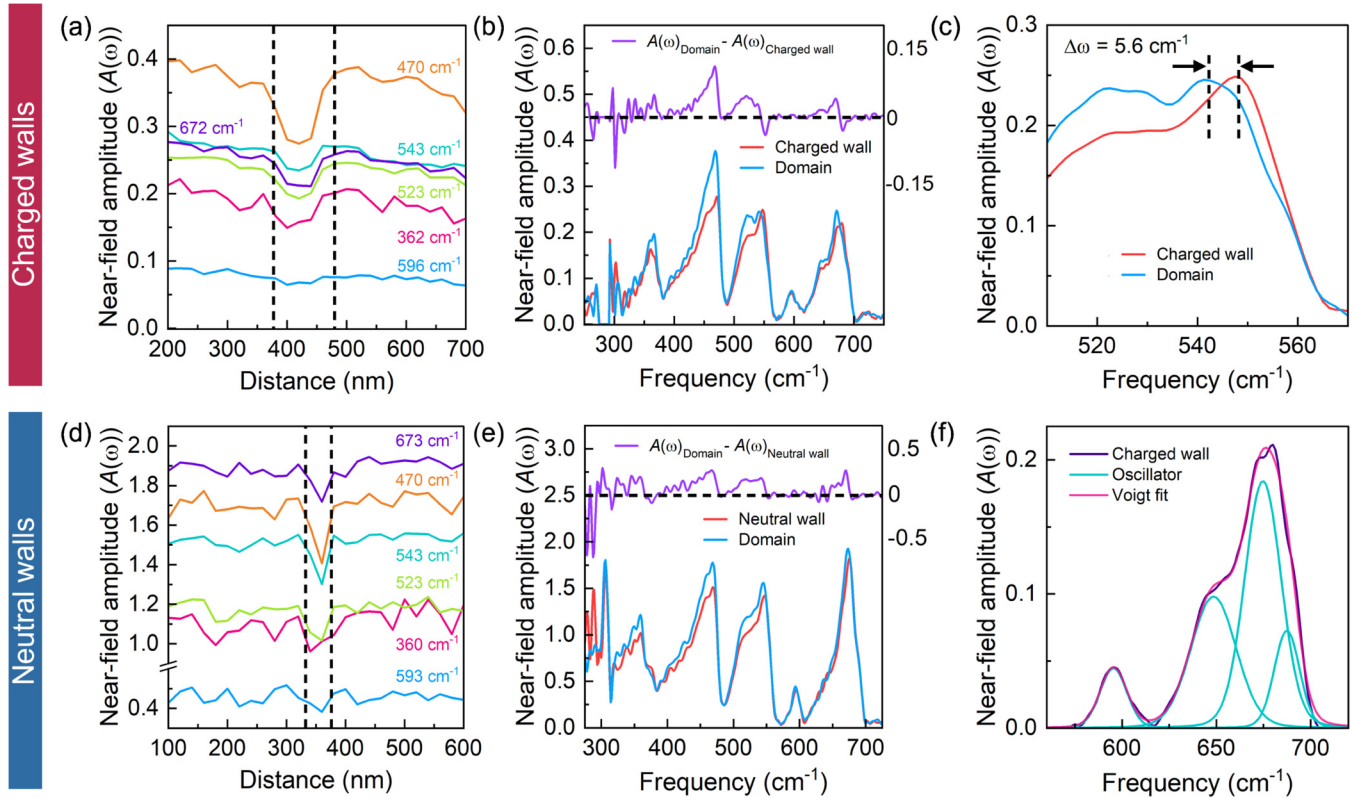
FIG. 4. Fixed frequency cuts of the *ab*- and *c*- walls (a) and (d) taken from the near-field infrared images of Ni$_3$TeO$_6$ in Fig. 3. Six distinct phonons are discernible from the contour plot. Five of these features display a marked amplitude decrease as the wall is crossed. Comparison of fixed distance cuts of the near-field image (b) and (e) from within the walls (red) vs the adjacent polar domains (blue). Difference spectra are plotted for clarity (purple). The *A* symmetry octahedral contraction and rotation around *c* at 543 cm^{-1} displays the most significant hardening and is emphasized in (c). (f) A representative oscillator fit from which we extract phonon lifetimes.

simpler to resolve, also improves reliability and provides a "proof of principle" that this technique has the potential to reveal such differences. Overall, we find that phonons in Ni$_3$TeO$_6$ host lifetimes on the order of 1 ps (Tables II and S1 in the supplementary material).

TABLE II. Representative phonon lifetimes and changes in lifetime are shown at both charged and neutral walls.

	ω (cm^{-1})	Charged wall		Neutral wall	
		τ_{ph} (ps)	$\Delta\tau_{ph}$ (%)	τ_{ph} (ps)	$\Delta\tau_{ph}$ (%)
Domain	596	0.37		0.43	
	645	0.19		0.14	
	672	0.27		0.24	
	688	0.37		0.77	
Domain wall	596	0.32	−13	0.37	−14
	645	0.19	0	0.12	−12
	672	0.23	−13	0.24	0
	688	0.34	−10	0.91	19

That said, there are significant modifications to certain phonon lifetimes at the neutral and charged walls. For instance, the change in the phonon lifetime ($\Delta\tau_{ph}$) for the axial stretching mode at 645 cm^{-1}, oriented along *c*, is on the order of 10% in the case of the neutral wall, whereas there is no appreciable difference for the charged walls. Alternately, $\Delta\tau_{ph}$ for the stretching mode associated with *ab*-plane contraction at 672 cm^{-1} is between 10% and 20% for the charged walls but negligible in the neutral walls. In both cases, $\Delta\tau_{ph}$ is essentially zero for modes oriented along the stiffer chiral interface. In the case of the neutral walls, the asymmetric octahedral stretching mode at 688 cm^{-1} also seems consistent with phonon lifetime increases at the wall.

IV. SUMMARY

In order to explore the properties of polar domain walls in a multiferroic with interlocked chirality and polarization, we employed synchrotron-based near-field infrared nano-spectroscopy to image the 180° charged and neutral interfaces in Ni$_3$TeO$_6$. Comparison of the contour, fixed distance, and fixed frequency plots reveals that charged walls are twice as wide as neutral walls

due to added strain created at the interface from on-end chiral helices. Additionally, neutral walls appear to display a lower energy cost of formation compared to their charged counterparts, supporting the idea that neutral walls are more energetically favorable in this system. The chirality is responsible for much of the stiffness at the interface and, therefore, the magnitude of the hardening of certain phonons at the wall. The largest frequency shift takes place in an octahedral contraction and rotation along c modifying the force constant by approximately 1%. Our estimates reveal that phonon lifetimes are on the order of 1 ps or less, with marked changes at the charged and neutral walls. The strained interface caused by the chiral helices may reduce the change in τ_{ph} of some modes at the wall.

SUPPLEMENTARY MATERIAL

See the supplementary material that contains additional details regarding the traditional far-field measurements, synchrotron-based near-field infrared methods, and the phonon lifetime calculations.

ACKNOWLEDGMENTS

AUTHOR DECLARATIONS
Conflict of Interest

The authors have no conflicts to disclose.

Author Contributions

Ashley M. Sargent: Conceptualization (equal); Data curation (equal); Formal analysis (equal); Investigation (equal); Validation (equal); Visualization (equal); Writing – original draft (equal); Writing – review & editing (equal). **Kevin A. Smith:** Conceptualization (supporting); Formal analysis (supporting); Validation (equal); Writing – review & editing (equal). **Xianghan Xu:** Resources (equal). **Kai Du:** Resources (supporting). **Sang-Wook Cheong:** Conceptualization (supporting); Resources (supporting); Writing – review & editing (supporting). **Lukas Wehmeier:** Resources (supporting). **G. L. Carr:** Resources (lead). **Janice L. Musfeldt:** Conceptualization (equal); Data curation (equal); Formal analysis (equal); Funding acquisition (lead); Investigation (equal); Project administration (equal); Resources (lead); Supervision (lead); Validation (equal); Writing – review & editing (equal).

DATA AVAILABILITY

The data that support the findings of this study are available from the corresponding author upon reasonable request.

REFERENCES

[1] J. Seidel, L. W. Martin, Q. He, Q. Zhan, Y.-H. Chu, A. Rother, M. E. Hawkridge, P. Maksymovych, P. Yu, M. Gajek, N. Balke, S. V. Kalinin, S. Gemming, F. Wang, G. Catalan, J. F. Scott, N. A. Spaldin, J. Orenstein, and R. Ramesh, "Conduction at domain walls in oxide multiferroics," Nat. Mater. **8**, 229–234 (2009).

[2] D. Meier and S. M. Selbach, "Ferroelectric domain walls for nanotechnology," Nat. Rev. Mater. **7**, 157–173 (2022).

[3] H.-Y. Zhang, X.-J. Song, X.-G. Chen, Z.-X. Zhang, Y.-M. You, Y.-Y. Tang, and R.-G. Xiong, "Observation of vortex domains in a two-dimensional lead iodide perovskite ferroelectric," J. Am. Chem. Soc. **142**, 4925–4931 (2020).

[4] G. Catalan, J. Seidel, R. Ramesh, and J. F. Scott, "Domain wall nanoelectronics," Rev. Mod. Phys. **84**, 119–156 (2012).

[5] A. Q. Jiang and Y. Zhang, "Next-generation ferroelectric domain-wall memories: Principle and architecture," NPG Asia Mater. **11**, 2 (2019).

[6] L. Li, J. Britson, J. R. Jokisaari, Y. Zhang, C. Adamo, A. Melville, D. G. Schlom, L. Chen, and X. Pan, "Giant resistive switching via control of ferroelectric charged domain walls," Adv. Mater. **28**, 6574–6580 (2016).

[7] Z. Luo, A. Hrabec, T. P. Dao, G. Sala, S. Finizio, J. Feng, S. Mayr, J. Raabe, P. Gambardella, and L. J. Heyderman, "Current-driven magnetic domain-wall logic," Nature **579**, 214–218 (2020).

[8] D. Kumar, H. J. Chung, J. Chan, T. Jin, S. T. Lim, S. S. P. Parkin, R. Sbiaa, and S. N. Piramanayagam, "Ultralow energy domain wall device for spin-based neuromorphic computing," ACS Nano **17**, 6261–6274 (2023).

[9] D. M. Evans, V. Garcia, D. Meier, and M. Bibes, "Domains and domain walls in multiferroics," Phys. Sci. Rev. **5**, 20190067 (2020).

[10] W. Wu, J. R. Guest, Y. Horibe, S. Park, T. Choi, S.-W. Cheong, and M. Bode, "Polarization-modulated rectification at ferroelectric surfaces," Phys. Rev. Lett. **104**, 217601 (2010).

[11] D. Meier, "Functional domain walls in multiferroics," J. Phys.: Condens. Matter **27**, 463003 (2015).

[12] M. G. Kim, H. Miao, B. Gao, S.-W. Cheong, C. Mazzoli, A. Barbour, W. Hu, S. B. Wilkins, I. K. Robinson, M. P. M. Dean, and V. Kiryukhin, "Imaging antiferromagnetic antiphase domain boundaries using magnetic Bragg diffraction phase contrast," Nat. Commun. **9**, 5013 (2018).

[13] Y. Kumagai and N. A. Spaldin, "Structural domain walls in polar hexagonal manganites," Nat. Commun. **4**, 1540 (2013).

[14] E. A. Nowadnick and C. J. Fennie, "Domains and ferroelectric switching pathways in $Ca_3Ti_2O_7$ from first principles," Phys. Rev. B **94**, 104105 (2016).

[15] Y. Sun, C. Lee, H.-Y. Yang, D. H. Torchinsky, F. Tafti, and J. Orenstein, "Mapping domain-wall topology in the magnetic Weyl semimetal CeAlSi," Phys. Rev. B **104**, 235119 (2021).

[16] C. Lee, P. Vir, K. Manna, C. Shekhar, J. E. Moore, M. A. Kastner, C. Felser, and J. Orenstein, "Observation of a phase transition within the domain walls of ferromagnetic $Co_3Sn_2S_2$," Nat. Commun. **13**, 3000 (2022).

[17] Q.-C. Sun, X. Xi, X. Wang, N. Lee, D. Mazumdar, R. J. Smith, G. L. Carr, S.-W. Cheong, and J. L. Musfeldt, "Spectroscopic signatures of domain walls in hexagonal $ErMnO_3$," Phys. Rev. B **90**, 121303 (2014).

[18] M. Fiebig, T. Lottermoser, D. Meier, and M. Trassin, "The evolution of multiferroics," Nat. Rev. Mater. **1**, 16046 (2016).

[19] X. Wu, K. Du, L. Zheng, D. Wu, S.-W. Cheong, and K. Lai, "Microwave conductivity of ferroelectric domains and domain walls in a hexagonal rare-earth ferrite," Phys. Rev. B **98**, 081409 (2018).

[20] H. A. Bechtel, E. A. Muller, R. L. Olmon, M. C. Martin, and M. B. Raschke, "Ultrabroadband infrared nanospectroscopic imaging," Proc. Natl. Acad. Sci. U.S.A. **111**, 7191–7196 (2014).

05 August 2025 16:01:18

[21]O. Khatib, H. A. Bechtel, M. C. Martin, M. B. Raschke, and G. L. Carr, "Far infrared synchrotron near-field nanoimaging and nanospectroscopy," ACS Photonics **5**, 2773–2779 (2018).

[22]H. A. Bechtel, S. C. Johnson, O. Khatib, E. A. Muller, and M. B. Raschke, "Synchrotron infrared nano-spectroscopy and -imaging," Surf. Sci. Rep. **75**, 100493 (2020).

[23]L. Wehmeier, M. Liu, S. Park, H. Jang, D. N. Basov, C. C. Homes, and G. L. Carr, "Ultrabroadband terahertz near-field nanospectroscopy with a HgCdTe detector," ACS Photonics **10**, 4329–4339 (2023).

[24]K. A. Smith, S. P. Ramkumar, K. Du, X. Xu, S.-W. Cheong, S. N. G. Corder, H. A. Bechtel, E. A. Nowadnick, and J. L. Musfeldt, "Real-space infrared spectroscopy of ferroelectric domain walls in multiferroic h-(Lu,Sc)FeO$_3$," ACS Appl. Mater. Interfaces **15**, 7562–7571 (2023).

[25]A. M. Sargent, K. A. Smith, K. Du, X. Xu, S.-W. Cheong, S. N. G. Corder, H. A. Bechtel, and J. L. Musfeldt, "Imaging ferroelastic domain walls in hybrid improper ferroelectric Sr$_3$Sn$_2$O$_7$," Nano Lett. **24**, 14460–14465 (2024).

[26]I. Živković, K. Prša, O. Zaharko, and H. Berger, "Ni$_3$TeO$_6$—A collinear antiferromagnet with ferromagnetic honeycomb planes," J. Phys.: Condens. Matter **22**, 056002 (2010).

[27]R. Becker and H. Berger, "Reinvestigation of Ni$_3$TeO$_6$," Acta Crystallogr. E **62**, i222–i223 (2006).

[28]X. Wang, F.-T. Huang, J. Yang, Y. S. Oh, and S.-W. Cheong, "Interlocked chiral/polar domain walls and large optical rotation in Ni$_3$TeO$_6$," APL Mater. **3**, 076105 (2015).

[29]Y. S. Oh, S. Artyukhin, J. J. Yang, V. Zapf, J. W. Kim, D. Vanderbilt, and S.-W. Cheong, "Non-hysteretic colossal magnetoelectricity in a collinear antiferromagnet," Nat. Commun. **5**, 3201 (2014).

[30]J. W. Kim, S. Artyukhin, E. Mun, M. Jaime, N. Harrison, A. Hansen, J. Yang, Y. Oh, D. Vanderbilt, V. Zapf, and S.-W. Cheong, "Successive magnetic-field-induced transitions and colossal magnetoelectric effect in Ni$_3$TeO$_6$," Phys. Rev. Lett. **115**, 137201 (2015).

[31]M. Yokosuk, H. Kim, K. Hughey, J. Kim, A. Stier, K. O'Neal, J. Yang, S. Crooker, K. Haule, S. Cheong, D. Vanderbilt, and J. Musfeldt, "Nonreciprocal directional dichroism of a chiral magnet in the visible range," npj Quantum Mater. **5**, 20 (2020).

[32]A. A. Sirenko, P. Marsik, L. Bugnon, M. Soulier, C. Bernhard, T. N. Stanislavchuk, X. Xu, and S.-W. Cheong, "Total angular momentum dichroism of the terahertz vortex beams at the antiferromagnetic resonances," Phys. Rev. Lett. **126**, 157401 (2021).

[33]K. Park, M. O. Yokosuk, M. Goryca, J. J. Yang, S. A. Crooker, S. W. Cheong, K. Haule, D. Vanderbilt, H. S. Kim, and J. L. Musfeldt, "Nonreciprocal directional dichroism at telecom wavelengths," npj. Quantum Mater. **7**, 38 (2022).

[34]P. E. Hopkins, C. Adamo, L. Ye, B. D. Huey, S. R. Lee, D. G. Schlom, and J. F. Ihlefeld, "Effects of coherent ferroelastic domain walls on the thermal conductivity and Kapitza conductance in bismuth ferrite," Appl. Phys. Lett. **102**, 121903 (2013).

[35]E. Langenberg, D. Saha, M. E. Holtz, J.-J. Wang, D. Bugallo, E. Ferreiro-Vila, H. Paik, I. Hanke, S. Ganschow, D. A. Muller, L.-Q. Chen, G. Catalan, N. Domingo, J. Malen, D. G. Schlom, and F. Rivadulla, "Ferroelectric domain walls in PbTiO$_3$ are effective regulators of heat flow at room temperature," Nano Lett. **19**, 7901–7907 (2019).

[36]Y. Pang, Y. Li, Z. Gao, X. Qian, X. Wang, J. Hong, and P. Jiang, "Thermal transport manipulated by vortex domain walls in bulk h-ErMnO$_3$," Mater. Today Phys. **31**, 100972 (2023).

[37]A. Negi, H. P. Kim, Z. Hua, A. Timofeeva, X. Zhang, Y. Zhu, K. Peters, D. Kumah, X. Jiang, and J. Liu, "Ferroelectric domain wall engineering enables thermal modulation in PMN–PT single crystals," Adv. Mater. **35**, 2211286 (2023).

[38]R. Sankar, G. J. Shu, B. K. Moorthy, R. Jayavel, and F. C. Chou, "Growing of fixed orientation plane of single crystal using the flux growth technique and ferrimagnetic ordering in Ni$_3$TeO$_6$ of stacked 2D honeycomb rings," Dalton Trans. **42**, 10439 (2013).

[39]A. S. McLeod, E. van Heumen, J. G. Ramirez, S. Wang, T. Saerbeck, S. Guenon, M. Goldflam, L. Anderegg, P. Kelly, A. Mueller, M. K. Liu, I. K. Schuller, and D. N. Basov, "Nanotextured phase coexistence in the correlated insulator V$_2$O$_3$," Nat. Phys. **13**, 80–86 (2017).

[40]K. A. Smith, E. A. Nowadnick, S. Fan, O. Khatib, S. J. Lim, B. Gao, N. C. Harms, S. N. Neal, J. K. Kirkland, M. C. Martin, C. J. Won, M. B. Raschke, S.-W. Cheong, C. J. Fennie, G. L. Carr, H. A. Bechtel, and J. L. Musfeldt, "Infrared nano-spectroscopy of ferroelastic domain walls in hybrid improper ferroelectric Ca$_3$Ti$_2$O$_7$," Nat. Commun. **10**, 5235 (2019).

[41]M. O. Yokosuk, S. Artyukhin, A. al Wahish, X. Wang, J. Yang, Z. Li, S.-W. Cheong, D. Vanderbilt, and J. L. Musfeldt, "Tracking the continuous spin-flop transition in Ni$_3$TeO$_6$ by infrared spectroscopy," Phys. Rev. B **92**, 144305 (2015).

[42]A. A. Govyadinov, I. Amenabar, F. Huth, P. S. Carney, and R. Hillenbrand, "Quantitative measurement of local infrared absorption and dielectric function with tip-enhanced near-field microscopy," J. Phys. Chem. Lett. **4**, 1526–1531 (2013).

[43]P. S. Bednyakov, B. I. Sturman, T. Sluka, A. K. Tagantsev, and P. V. Yudin, "Physics and applications of charged domain walls," npj Comput. Mater. **4**, 65 (2018).

[44]C. Stefani, L. Ponet, K. Shapovalov, P. Chen, E. Langenberg, D. G. Schlom, S. Artyukhin, M. Stengel, N. Domingo, and G. Catalan, "Mechanical softness of ferroelectric 180° domain walls," Phys. Rev. X **10**, 041001 (2020).

[45]Y. Ma, G. Zhong, Z. Dai, and Q. Ou, "In-plane hyperbolic phonon polaritons: Materials, properties, and nanophotonic devices," npj Nanophoton. **1**, 25 (2024).

[46]B. Wei, X. Zhang, W. Li, J. Li, Y. Li, Q. Gao, J. Hong, C.-W. Nan, and Y.-H. Lin, "Optical phonons on thermal conduction in advanced materials," Appl. Phys. Rev. **12**, 011324 (2025).

[47]N. Varela-Domínguez, M. S. Claro, C. Vázquez-Vázquez, M. A. López-Quintela, and F. Rivadulla, "Electric-field control of the local thermal conductivity in charge transfer oxides," Adv. Mater. **37**, 2413045 (2025).

[48]Q. C. Sun, D. Mazumdar, L. Yadgarov, R. Rosentsveig, R. Tenne, and J. L. Musfeldt, "Spectroscopic determination of phonon lifetimes in rhenium-doped MoS$_2$ nanoparticles," Nano Lett. **13**, 2803–2808 (2013).

05 August 2025 16:01:18